On momentum transfer and external work done to clamped elasto-plastic beams in an air blast

Y. Yuan[1,2], P. J. Tan[1*], K. A. Shojaei[1‡], P. Wrobel[1]

[1] *Department of Mechanical Engineering, University College London, Torrington Place, London WC1E 7JE, UK*

[2] *State Key Laboratory of Automotive Safety & Energy, Department of Automotive Engineering, Tsinghua University, Beijing 100084, China*

Abstract

This paper revisits a classical fluid-structure interaction problem on the momentum transfer and external work done to structures by a blast wave propagating in a nonlinear compressible medium (air). A fully-clamped ductile beam system is considered here, in place of the rigid free-standing plate used in the KNR theory (Kambouchev et al., 2006, 2007), which takes into account limits to material deformation, boundary compliance and boundary failure. The model is used to critically re-evaluate the impulse imparted to the beam, and the subsequent external work done by a blast wave, for different modes of the beam deformation compared to its free-standing counterpart of identical mass per unit area (considered previously by others). It will be shown that the maximum beam deflection, transmitted impulse and external work done by the interface pressure are insensitive to FSI effects if loading is sufficient severe to induce boundary failure. Comparisons are also made between the structural performance of the beam system during fluid structure interaction in a compressible and incompressible fluid medium.

Keywords: Fluid-structure interaction, air blast, external work done and momentum transfer, damage, large deformation

1. Introduction

It is well-known that, in the acoustic limit, the impulse imparted to a rigid free-standing plate depends only on a non-dimensional FSI (fluid-structure interaction) parameter which

‡Now at DuPont Performance Materials, DuPont, Wilmington, Delaware, 19805, USA.

*Corresponding author

Email addresses: ucemyyu@ucl.ac.uk (Y. Yuan[1,2]), pj.tan@ucl.ac.uk (P. J. Tan[1])

is independent of the intensity of the blast – a direct consequence of the linearity assumption in Taylor's pioneering work [1]. This was subsequently extended by Kambouchev et al. [2, 3],

Nomenclature

A	Cross-sectional area of beam
B	Width of beam
c_a	Ambient air speed
C_R	Reflected coefficient
d	Standoff distance
d_0	Length of compressed air container
D	Damage variable
e	Internal energy of air particles
$\bar{E}^F$	Maximum non-dimensional external work done to a freestanding beam
E^D	External work done by interface pressure
$\bar{E}^D$	Maximum non-dimensional external work done by interface pressure
E_i	Incident energy of blast wave per unit area
F	Deformation gradient
H	Thickness of beam
zI_i	Incident impulse per unit area
I^T	Transmitted impulse
$\bar{I}^F$	Maximum total impulse per unit area of rigid free-standing beam
$\bar{I}^T$	Non-dimensional maximum transmitted impulse
I^*	Non-dimensional impulse
K_1, K_2	Coefficients for artificial viscosity
K_ϕ	Rotational spring stiffness
L	Half length of beam member
M_0	Fully plastic bending moment
$\bar{M}$	non-dimensional bending moment ($\triangleq M/M_0$)
N	Membrane force
N_0	Fully plastic membrane force
$\bar{N}$	non-dimensional membrane force ($\triangleq N/N_0$)
p_a	Ambient pressure
p_s	Peak incident overpressure
p_R	Reflected overpressure
p_{Int}	Interface overpressure
Q	Transverse shear force
Q_0	Fully plastic shear force
$\bar{Q}$	non-dimensional transverse shear force ($\triangleq Q/Q_0$)
t_1, t_2, t_3	Termination time of Phases I, II and III
t_i	Decay constant
U_s	Shock speed

v_0	Peak initial velocity
$\bar{W}$	Displacement ratio
W_0	Maximum mid-span deflection
W_B, W_S	Deflection at mid-span and support
Z	Lagrangian coordinate
β	Ratio of the plastic shear energy to total plastic work done
β_c	Critical value of β governing transition from mode II and III
β_s	FSI index
ΔE_0	Initial energy of compressed air container
γ_a	Specific heat ratio of air
ω_d, ω_s	State variable for damage and shear criteria
$\phi_i(x)$	Admissible mode function
ρ	Density of beam material
ρ_s	Gas density behind the shock front
ξ	Position of travelling plastic hinge

denoted as KNR hereinafter, to account for the effects of nonlinear fluid compressibility, such as in an air-blast loading of structures. A universal empirical formula expressed as a function of the generalised FSI parameter and blast intensity – a compressible counterpart of Taylor's original FSI index – was derived that predicts the transmitted impulse for a complete range of blast and plate characteristics. Predictions were shown to match exactly the asymptotic solution for the very heavy and very light rigid plates. The KNR theory revealed that nonlinear fluid compressibility further enhances the beneficial effects of FSI in reducing the impulse that was imparted. However, it is unclear to what extent the aforesaid would be altered when considering more realistic structures that experience limits to material deformation, boundary compliance and failure – this is to be investigated in this paper using a fully clamped, elasto-plastic beam system.

Hutchinson [4] proposed an alternative FSI parameter (defined in terms of invariants of the incident wave) to elucidate the role of backing to an adiabatically compressed air layer and the effects of standoff on the external work done by, and momentum transfer from, a blast wave to a structure. A massive plate was shown to always acquire twice the amount of momentum of the incident wave and that standoff was found to have a significant effect in attenuating the external work done by the interface pressure on the plate. Again, this study considers a rigid free-standing plate structure within a one-dimensional context.

More recently, Subramaniam et al. [5] investigated the response of elastic structures in air blasts, where the former is idealised as a lumped-mass with a linear backing spring that offers resistance to transverse deformation arising from material deformation and boundary constraints. They found that the error in the predicted maximum displacement, both with and without FSI, is directly proportional to the ratio of the velocity of the structure to the speed of the shock (blast) wave. However, their model is limited to elastic structural

response and the prediction error would increase if the blast loading is sufficiently intense, as is often the case, to induce significant plastic (membrane-type) deformation leading to, in extreme cases, a loss of structural integrity. Follow-on work by the same authors [6] on the air blast loading of flexible foams, again in a one-dimensional context, found that the error arising from ignoring FSI effect is significant only in the early stages of the blast pressure history where motion of the foam produces a reduction in interface overpressure; this error is largest in the 'weaker' foams as they tend to acquire a higher acceleration away from the blast wave.

In this paper, an elasto-plastic beam system is used in place of the idealised 'rigid structure' to reconsider the fluid structure interaction problem. A model of the ductile beam system – previously developed by Yuan et al. [7] – is used here, which is capable of capturing the different modes of beam deformation (observed in blast experiments), the initiation and evolution of damage with increasing transverse beam deflection, and its consequential detachment from the support. The same numerical approach by Hutchinson [4] is employed to generate an exponentially decaying pressure wave with a peak overpressure that attenuates naturally with distance. By coupling the air domain to the ductile beam system, the momentum transfer from, and external work done by, the blast to a clamped ductile beam will be critically re-evaluated up until the point of beam detachment (or failure) from its boundary. Comparisons will also be made between the structural performance of the beam system in a compressible (this paper) and incompressible (from [8]) fluid medium as a result of fluid structure interaction.

The outline of this paper is as follows: Section 2 provides a succinct summary of the salient features in a ductile beam model by Yuan et al. [7], and describes the fluid and structure coupling scheme; results for the dynamic response of the ductile beam, considering fully-coupled FSI effects, are presented in Section 4; Section 5 establishes the conditions under which FSI cannot be ignored; results for the rigid free-standing and elasto-plastic beams are compared and sensitivity analyses carried out to elucidate the dependence of the model predictions on the beam's aspect ratio and inertial mass in Section 6; finally, Section 7 compares the performance of the beam system for air and underwater blasts.

2. Analytical model

The analytical model of a ductile beam system by Yuan et al. [7] is summarised here. For completeness, the numerical method that is employed to simulate air shock formation, its propagation and attenuation; and the coupling strategy (in time domain) to treat interactions between the shock wave and the aforesaid ductile beam model are also briefly outlined - both are identical to that employed in the original KNR studies [2, 3] and by Hutchinson [4].

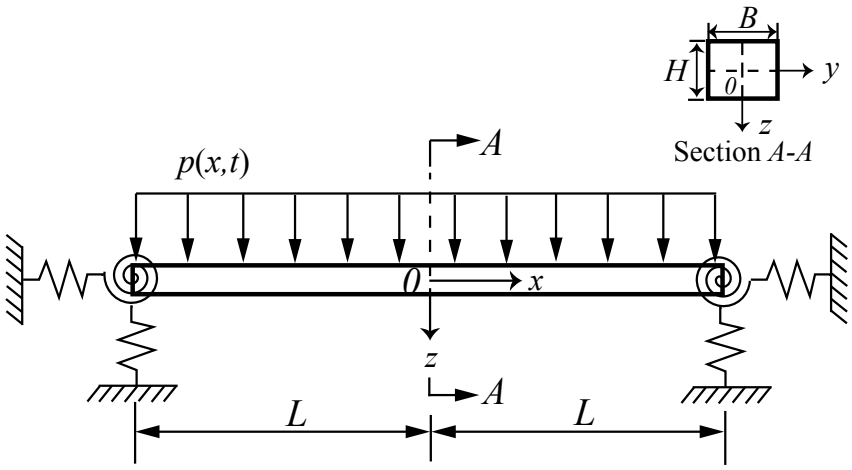

Figure 1: Schematic of the ductile beam system by Yuan et al. [7].

2.1. Model formulation [7]

A schematic of the ductile beam system that is modelled is given in Fig 1. It comprises of a slender beam (made of a rate-independent, elastic perfectly-plastic material) supported at each end by three springs, one rotational and two axials. The two torsional 'elasto-plastic' springs model the end rotation of the beam and the subsequent formation of plastic hinges. Both axial and vertical springs have 'rigid-plastic' characteristics to model plastic stretch and plastic shear sliding at the support, respectively. An air-shock pulse $p(t)$, is assumed to always impinge normally, and uniformly, over the full span of the beam regardless of its subsequent transverse 'in-plane' motion.

The beam deformation is divided into three phases according to the sequence of hinge formation: (a) Phase 1 ($0 < t \leq t_1$) - no plastic hinge forms anywhere along the beam; (b) Phase II ($t_1 < t \leq t_2$) - a stationary plastic hinge forms at the support on each end of the beam; (c) Phase III ($t_2 < t \leq t_3$) - plastic hinge travels from the support towards, and coalesce with, an existing stationary hinge at the mid-span, ending in a final three-hinge collapse configuration. An interactive yield criterion that combines the bending moment M, membrane force N and the transverse shear force Q given by

$$|\bar{M}|\sqrt{1-\bar{Q}^2}+\bar{N}^2+\bar{Q}^2-1=0 \tag{1}$$

is adopted, where $\bar{M}$, $\bar{N}$ and $\bar{Q}$ are the non-dimensional generalised stresses. In each phase, the transverse beam deflection is approximated as a sum of n generalised displacements $w_i(t)$ and admissible mode functions $\phi_i(x)$. Once the total strain energy V of each phase is derived, the governing equations of motions for the beam system are obtained by substituting the Lagrangian into the well-known Euler-Lagrange equation – see details given in [7]. The general equation of motion is expressed by

$$\sum_{j=1}^{n} M_{ij}\ddot{w}_j+\frac{\partial V}{\partial w_i}=Bp(t)\int_0^L \phi_i(x)\mathrm{d}x, \quad i=1,2,...,n. \tag{2}$$

where M_{ij} is the generalised mass and $p(t)$ is the pulse pressure loading.

The model implements gradual softening of the non-dimensional bending moment $\bar{M}$, membrane force $\bar{N}$ and transverse shear force $\bar{Q}$ as a function of effective strain ϵ_{eff}. Initiation of ductile damage follows a criterion given by

$$\omega_d = \frac{\epsilon_{\text{eff}}}{\epsilon_d} = 1 \tag{3}$$

where ω_d is a state variable that increases monotonically with the effective strain ϵ_{eff}, and ϵ_d is the effective strain at damage initiation (also known as damage strain). Beyond this, progressive softening of the generalised stresses occur in accordance to the following evolution law:

$$|\bar{M}| = |\bar{M}^f|(1-D), \quad \bar{N} = \bar{N}^f(1-D) \quad \text{and} \quad \bar{Q} = \bar{Q}^f(1-D) \tag{4}$$

where $\bar{M}^f$, $\bar{N}^f$ and $\bar{Q}^f$ are the non-dimensional generalised stresses at the onset of damage, respectively. For simplicity, a linear evolution of the damage variable D with effective strain ϵ_{eff} given by

$$D = \frac{\epsilon_{\text{eff}} - \epsilon_d}{\epsilon_r - \epsilon_d} \tag{5}$$

is implemented where ϵ_r is the rupture strain of the beam material. The non-dimensional generalised stresses reduce to zero when $D = 1$ at which point *failure* (complete detachment from the supports) occurs.

The three distinct deformation régimes identified by Menkes and Opat [9] are delineated in accordance to the following criteria:

$$\text{Mode I}: \quad D < 1, \quad \omega_s < 1 \tag{6a}$$

$$\text{Mode II}: \quad D = 1, \quad \omega_s < 1 \tag{6b}$$

$$\text{Mode III}: \quad D = 1, \quad \omega_s \geq 1 \tag{6c}$$

where the state variable ω_s is given by

$$\omega_s = \frac{\beta}{\beta_c}. \tag{7}$$

In Eq 7, β is the ratio of the plastic work absorbed through shearing deformation to the total plastic work done and β_c (=0.45) [10] is a critical value delineating the transition between modes II to III. Table 1 lists the material properties - they are rate-insensitive - for the Aluminium 6061-T6 beams that were modelled.

2.2. Coupling of fluid domain to the structure

The coupling problem consists of an 'air-column' of two parts, viz. 'compressed container' of adiabatic air and quiescent ambient air, and an elasto-plastic beam system of Fig. 2.

Table 1: Material properties of the Aluminium (6061-T6) beam [9]

Density, ρ (kg/m^3)	Young's modulus, E (GPa)	Static yield strength, σ_Y (MPa)	Poisson's ratio	Damage strain, ϵ_d	Rupture strain, ϵ_r
2686	69	283	1/3	0.38	0.5

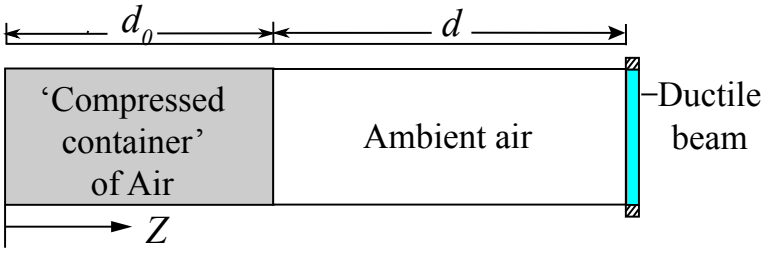

Figure 2: Schematic of FSI model in air

Following Hutchinson [4], the 'compressed container' of air in the interval $0 \leq Z \leq d_0$ is prescribed an initial velocity distribution of

$$v(Z) = v_0 e^{-(Z/d_0)^2} \tag{8}$$

where Z is the Lagrangian coordinate, d_0 is the length of the compressed air container and v_0 is the peak velocity. Hence, the compressed air has a density distribution $\rho(Z)$ and a finite initial energy per unit area ΔE_0 given by [4]

$$\begin{aligned} \frac{p(Z)}{p_a} &= \left[\frac{\rho(Z)}{\rho_a}\right]^{\gamma_a} = \left[1 + \frac{\gamma_a - 1}{2}\left(\frac{v(Z)}{c_a}\right)^2\right]^{\gamma_a/(\gamma_a - 1)} \quad \text{and} \\ \Delta E_0 &= \frac{p_a d_0}{\gamma_a - 1}\left[\left(1 + \frac{\gamma_a - 1}{2}\left(\frac{v_0}{c_a}\right)^2\right)^{\gamma_a/(\gamma_a-1)} - \left(1 + \frac{\gamma_a - 1}{2}\left(\frac{v_0}{c_a}\right)^2\right)^{1/(\gamma_a-1)}\right] \end{aligned} \tag{9}$$

where γ_a (= 1.4) is the specific heat ratio of air, p_a (= 104761 Pa) is the ambient pressure, ρ_a (= 1.225 kg/m^3) is the density of air, c_a (= 346 m/s) is speed of sound in air and the subscript 'a' denotes ambient conditions. At time $t = 0$, the container of air is 'released' and a shock wave (of an exponentially decaying type) is generated which propagates towards the beam. In this study, the negative suction phase of a blast pulse is not considered. It is worth emphasising that the FSI problem is modelled here in an idealised one-dimensional context - this follows the approach of existing studies [5, 6, 11]. Consequently, it does not account for any interface pressure variations along the beam surface in the longitudinal direction ($x-$ direction in Fig. 1). Even though this is likely to lead to quantitative inaccuracies, by over-predicting the effects of FSI in alleviating the interface pressure, it should not, qualitatively, influence the general outcome of the current findings.

The equations governing fluid motion (in both the 'compressed' container and ambient air) are expressed in a Lagrangian framework and consists of the following [2–4]:

1. The kinematic relations for the material velocity v and acceleration a are

$$v = \frac{\partial x_e}{\partial t} \quad \text{and} \quad a = \frac{\partial v}{\partial t} \tag{10}$$

where the Eulerian coordinate x_e, velocity v and acceleration a of a fluid particle are functions of Lagrangian coordinate Z and time t.

2. The momentum conservation equation is

$$\rho_0 a = -\frac{\partial p}{\partial Z} \tag{11}$$

where ρ_0 is the initial density of the particle with Lagrangian coordinate Z.

3. The equation of state was modified, by adding a viscous dissipation term Θ, to give [12]

$$p = (\gamma_a - 1)\rho_0 \frac{e}{F} - \Theta \tag{12}$$

where e is the internal energy, $F(= \partial x_e/\partial Z)$ is the deformation gradient; and, the viscous term Θ is included to stabilise the numerical scheme according to

$$\Theta = \begin{cases} -\rho_a (K_1 \dot{d}\Delta)^2 - \rho_a c_a K_2 |\dot{d}|\Delta, & \dot{d} < 0 \\ 0, & \dot{d} \geq 0 \end{cases} \tag{13}$$

where $\dot{d} = (1/F)\partial F/\partial t$ is the deformation rate, K_1 and K_2 are artificial viscosity coefficients and Δ is width of the shock wave (set as the grid spacing for numerical stability).

4. The energy conservation equation is

$$\frac{\partial e}{\partial t} = \left[(1 - \gamma_a)e + \frac{\Theta}{\rho_c}\right] \tag{14}$$

where ρ_c is the current density of the air particles.

The staggered method is adopted for the fluid-structure coupling in time domain [13, 14]. Interactions between the shock wave and elasto-plastic beam is achieved through enforcing the congruence conditions of velocity and displacement at the fluid-structure interface, i.e. the interface velocity and displacement must be identical for both the fluid and the structure. Following [5] and [8], the mid-span of the beam is evaluated through coupling to the one-dimensional air column. The governing equations (Eqs. 10, 11, 12 and 14), together with the initial conditions (Eqns. 8 and 9) and artificial viscosity (Eq. 13), are solved using the von Neumann-Richtmyer scheme which is based on a finite difference discretisation of the governing equations [12]. Starting at a current time step, when the state of the fluid and structure are known, the fluid-structure system is integrated in time to obtain the solution at the next time step as follows:

1. The current displacement at the fluid-structure interface is used in the governing equations of the fluid motion, i.e. Eqns. (10), (11), (12) and (14), to calculate the interface overpressure p_{Int} for the next time step.
2. The mid-span beam displacement at the next time step is updated by solving the equations of motion for the beam, subjected to the new interface overpressure $p_{\text{Int}}(t) = p(Z = d + d_0, t) - p_a$ obtained from step 1, given by

$$\sum_{j=1}^{n} M_{ij}\ddot{w}_j + \frac{\partial V}{\partial w_i} = Bp_{\text{Int}}(t)\int_0^L \phi_i(x)\mathrm{d}x, \quad i = 1, 2, ..., n. \tag{15}$$

Details of the finite difference scheme are well documented in the literature [3, 12, 15] and is not repeated here.

3. Validation of the numerical implementation (for air column)

To validate the numerical implementation of the air column (recall that the model of the structural beam was previously validated in [7]), we consider the normal reflection of a uniform shock from a fixed rigid wall where analytical solutions already exist. In a compressible medium, such as air, the reflected peak overpressure from a rigid wall takes the form of [16]

$$p_r = C_R p_s \tag{16}$$

where the reflected coefficient C_R are obtained from the well-known Rankine-Hugoniot relationships to give

$$C_R = \frac{8p_s/p_a + 14}{p_s/p_a + 7}. \tag{17}$$

For small p_s/p_a (the acoustic range), $C_R \simeq 2$; whilst, for $p_s/p_a \gg 1$, $C_R \to 8$.

Figures 3a and 3b plot the incident $p_I(t)$ and reflected $p_R(t)$ overpressure-time histories – the latter from a fixed rigid wall – generated for two different blast intensities at various standoff distance d, using the numerical scheme summarised in Section 2.2. Nonlinear compressibility of air causes significant attenuation of the blast pulse, leading to a reduction in the peak overpressure of the evolving pressure pulse, and a corresponding increase in pulse duration t_d, with propagation distance. Figure 4 compares the normalised peak reflected overpressure (p_r/p_s) obtained numerically (the values were extracted from Figs. 3a and 3b for different standoff distance d/d_0) to the corresponding pressure reflection coefficient C_R predicted by Eq. (17). They are in excellent agreement for a wide range of shock intensities, suggesting that the numerical scheme used to generate shock in the air column was correctly implemented.

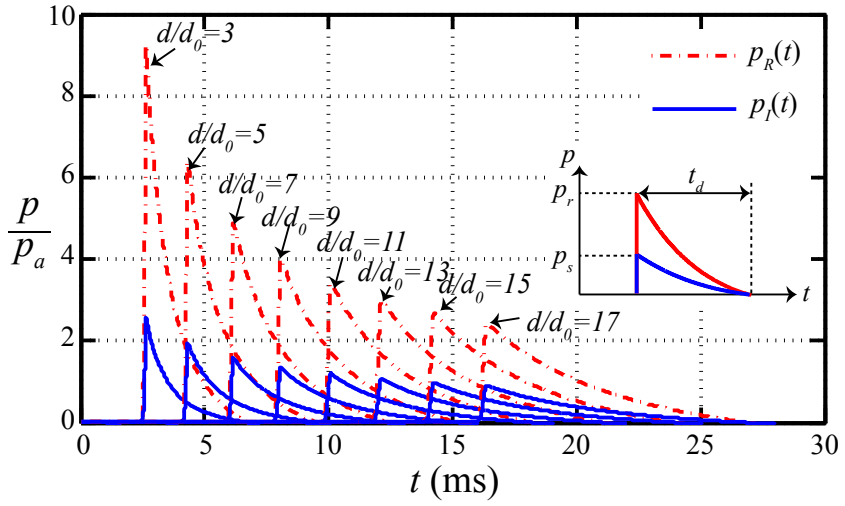

(a)

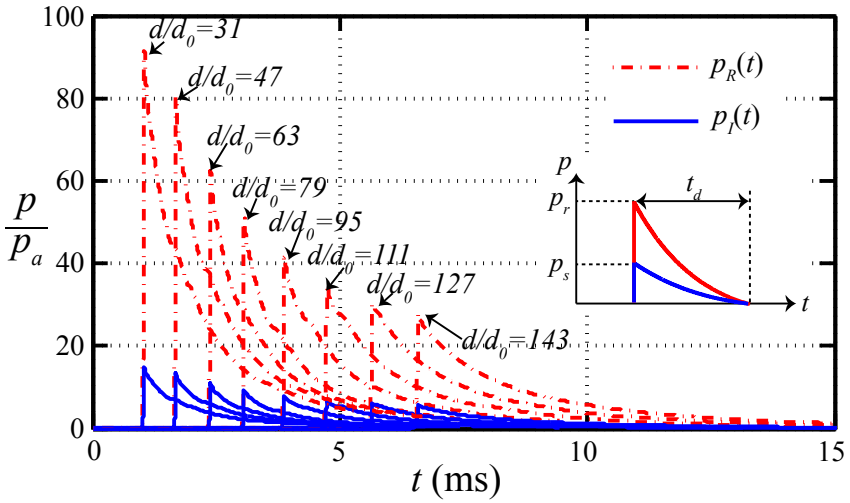

(b)

Figure 3: Incident $p_I(t)$ and reflected $p_R(t)$ overpressure-time histories for a shock interacting with a rigid wall at different standoff distance d: (a) 'weak' shock wave (using $v_0/c_a = 1.7$ and $d_0 = 0.5$ m in Eqs. 8-9) ; (b) 'strong' shock wave (using $v_0/c_a = 5.1$ and $d_0 = 0.05$ m in Eqs. 8-9) .

4. Dynamic response, with and without FSI, in different modes

In this section, analytical models of the air column and structural beam are used to compare the external work done by the interface pressure and momentum transfer to a typical beam deforming in three different modes in uncoupled (without FSI) and fully-coupled (with FSI) simulations.

The temporal history of the transmitted impulse per unit area $I^T(t')$ and external work done

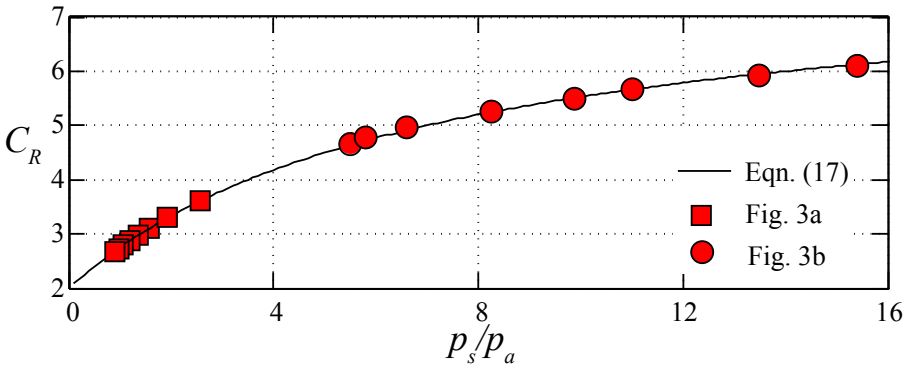

Figure 4: Comparison of the normalised peak reflected overpressure p_r/p_s obtained numerically (plotted previously in Figs. 3a and 3b) to the corresponding pressure reflection coefficient C_R predicted by Eq. (17).

per unit area $E^D(t')$ to the beam are given by

$$I^T(t') = \int_0^{t'} p_{\text{Int}}(t')\text{d}t' \tag{18}$$

and

$$E^D(t') = \frac{1}{BL}\int_0^L p_{\text{Int}}(t')W(x,t')\text{d}x. \tag{19}$$

They are normalised by the incident impulse I_i and energy E_i respectively, given by [3]

$$I_i = \int_0^{t_d} p_s\varphi(t')dt' = p_s t_i \quad \text{and} \tag{20}$$

$$E_i = p_s^2 t_i/\rho_a c_a \tag{21}$$

where t_i is the decay constant of the incident wave and t_d is the pulse duration. Note that time t' in Eqs. 18-20 is measured from when the pressure wave first arrives at the fluid-structure interface. It is worth emphasising that if the structural system fails (i.e. complete detachment occurs at $t' = t'_3$) before all its kinetic energy is expended, then the beam member would have a residual kinetic energy at the point of severance. Parts of this are absorbed through further plastic deformation as the beam member continues to deform until it reaches permanent set whilst the remaining as translational kinetic energy. Since fluid-structure interaction in the 'pre-detachment' régime is of interest, the 'post-detachment' response of the beam is not considered, or characterised, here.

Figure 5a plots the pressure, deflection, impulse and energy histories for a 0.17 m (L) $\times$ 0.01 m (H) $\times$ 0.01 m (B) beam subjected to a blast wave generated using the following parameters so that it deforms in mode I: $d_0 = 0.05$ m, $d/d_0 = 79$ and v_0/c_a=5.1. Note that in the uncoupled case, the interface pressure $p_{\text{Int}}(t')$ is the reflected overpressure time history from a stationary rigid wall obtained using the same incident blast pulse, this is denoted hereinafter by $p_R(t')$. The results reveal t'_3 – defined as the time taken to reach the maximum

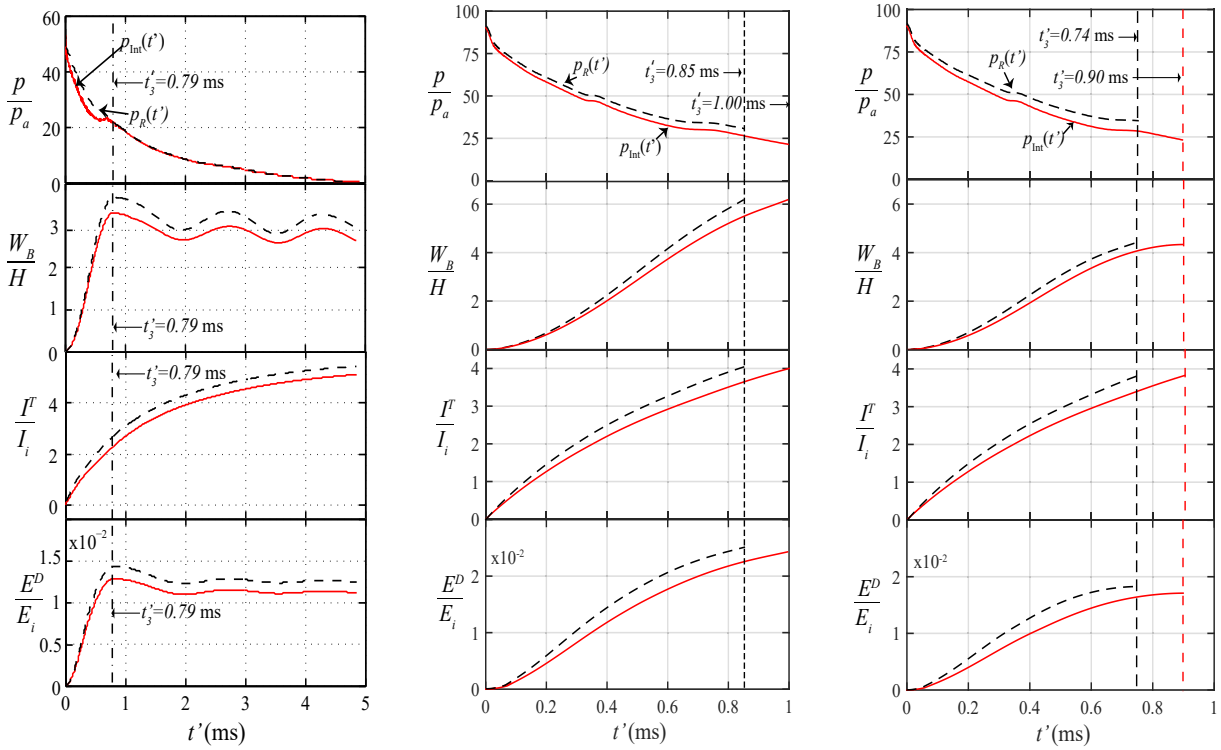

(a) Mode I ($d_0 = 0.05$ m, $d/d_0 = 79$ and v_0/c_a=5.1)

(b) Mode II ($d_0 = 0.05$ m, $d/d_0 = 31$ and v_0/c_a=5.1)

(c) Mode III ($d_0 = 0.05$ m, $d/d_0 = 31$ and v_0/c_a=5.1)

Figure 5: Interface pressure, mid-span deflection, transmitted impulse and external work done by the interface pressure for uncoupled (without FSI) and coupled (with FSI) beam response during (a) mode I (0.17 m × 0.01 m × 0.01 m), (b) mode II (0.2 m × 0.01 m × 0.01 m) and (c) mode III (0.17 m × 0.01 m × 0.01 m) deformation. - - denotes without FSI; — denotes with FSI. t_3' refers to the instant when beam motion ceases (if in mode I) or when failure (if in modes II or III) occurs.

mid-span beam deflection – to be an important time-scale for a beam deforming in mode I. When $t' \leq t_3'$, the interface overpressure $p_{\text{Int}}(t')$ is consistently lower in the coupled (with FSI) analysis compared to its uncoupled (without FSI) counterpart. This is due to rapid initial beam motion, as opposed to the stationary rigid wall, which results in alleviation of the interface overpressure in the former. By contrast, beyond $t' > t_3'$, there is no noticeable difference between the two interface pressure-time histories (with and without FSI) after the maximum beam deflection is reached. The reason is that, during the subsequent elastic rebound, the velocity of the beam is so insignificant that it hardly has any effect on the interface pressure $p_R(t')$ [5]. In mode I, where beam failure does not occur, the consequence of FSI is that the maximum beam deflection (mid-span), maximum transmitted impulse and the maximum external work done by the interface pressure are always lower compared to its uncoupled counterpart where FSI is ignored.

Figures 5b and 5c plot the same for beams deforming in mode II and III, respectively. It is important to note that $t = t_3'$ corresponds to the instant when complete beam detachment

(or failure) occurs at which point the simulation terminates. Results were shown for two beam geometries, viz. 0.2 m (L) $\times$ 0.01 m (H) $\times$ 0.01 m (B) and 0.17 m (L) $\times$ 0.01 m (H) $\times$ 0.01 m (B), subjected to an identical blast pulse ($d_0 = 0.05$ m, $d/d_0 = 31$ and v_0/c_a=5.1). Unlike in mode I, their interface overpressure $p_{\text{Int}}(t')$ is always lower than its uncoupled counterpart $p_R(t')$ throughout. Again, this is caused by rapid motion of the beam prior to the onset of failure which relieves the interface overpressure. Consequently, at every time t', the temporal mid-span deflection $W_B(t')/H$, transmitted impulse $I^T(t')/I_i$ and external work done $E^D(t')/E_i$ is also greater for the uncoupled case compared to its coupled counterpart - an observation which is broadly similar to mode I (see Fig. 5a). However, their corresponding peak value (this occurs at the point of beam failure) appears largely unaffected by whether or not FSI is considered. The reason is because a beam only fails when it reaches a critical maximum mid-span deflection and is independent of the pulse shape [7]. Hence, the temporal mid-span deflection $W_B(t')/H$ of the coupled analysis is able to increase for longer, compared to its uncoupled counterpart, before the onset of failure. The longer loading duration permits the transmitted impulse and external work done to make up for its earlier deficiency caused by FSI. Therefore, an uncoupled analysis suffices to determine the maximum value of the beam deflection, transmitted impulse and external work done by the interface pressure if a beam is deforming in either mode II or III since these quantities are insensitive to whether FSI is considered or not.

It is worth emphasising that the beam dimensions and loading parameters used to generate Fig 5 were deliberately chosen so that $t' = t'_3$ – this corresponds to the cessation of beam motion if in mode I or to failure if in mode II or III – is less than the positive duration of the incident pressure pulse, i.e. $t'_3 < t_d$. This is to highlight the differences between the predictions, with and without FSI, since results to be presented later in Section 5 will show that FSI effects are more significant for non-impulsive loadings, i.e. $t'_3/t_d < 1$.

5. Importance of FSI in mode I

Results in Section 4 have shown that the maximum mid-span deflection, transmitted impulse and external work done by the interface pressure are only sensitive to FSI if the beam is deforming in mode I, i.e. when beam failure does not occur. Therefore, an interesting follow-up question to address is: Given that a beam deforms in mode I, what parameters (and to what extent do they) control its sensitivity to FSI? The predicted mid-span beam deflection [5] is commonly used as an indicator to compare predicted structural response, with and without FSI. Here, we introduce a displacement ratio defined as $\bar{W} = W_0^{\text{FSI}}/W_0^{\text{NO FSI}}$ to provide a measure of the error that arises from neglecting FSI. Since error is given by $1-\bar{W}$, a decreasing $\bar{W}$ corresponds to an increase in predicted error. Note that the reflected overpressure history $p_R(t)$ from a stationary rigid wall, see Section 4, is used to obtain $W_0^{\text{NO FSI}}$.

Figures 6, 7 and 8 show the variation of displacement ratio $\bar{W}$ as functions of velocity ratio $v_{\max}/U_s$, time ratio t_3/t_d and β_s ($\triangleq \rho_s U_s t_i/\rho H$ - Kambouchev's FSI index), respectively,

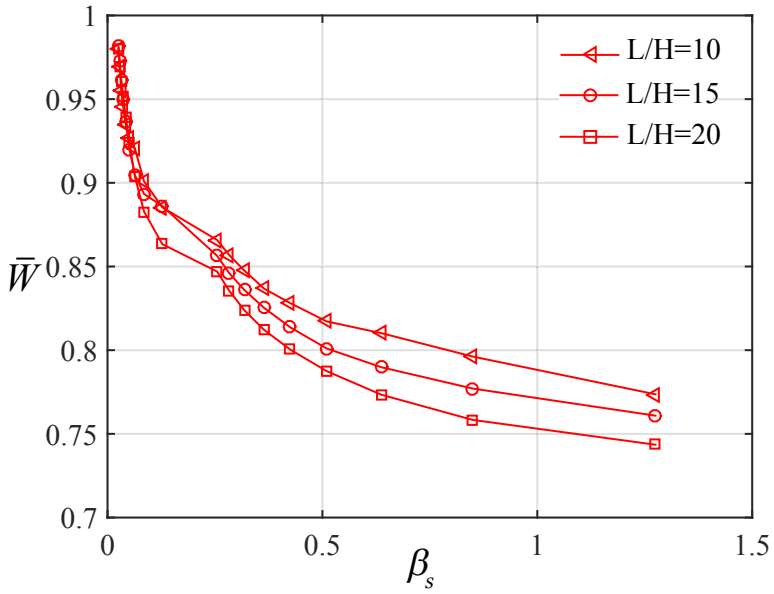

Figure 6: Variation of the displacement ratio $\bar{W}$ with velocity ratio $v_{\max}/U_s$ for beams of different aspect ratio L/H deforming in mode I.

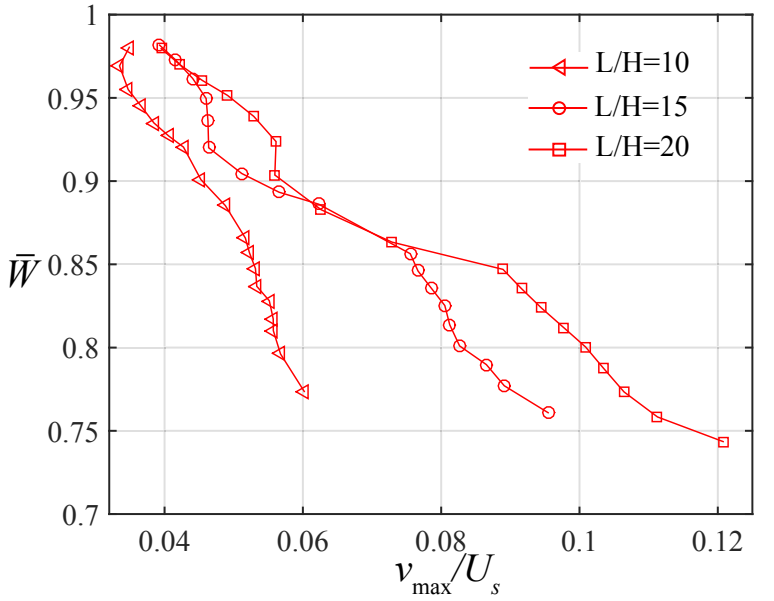

Figure 7: Variation of the displacement ratio $\bar{W}$ with time ratio t_3'/t_d for beams of different aspect ratio L/H deforming in mode I.

where $v_{\max}$ is the maximum mid-span velocity expressed as

$$v_{\max} = \max_{0 \le t' \le t_3'} [\dot{W}(x = 0, t')], \tag{22}$$

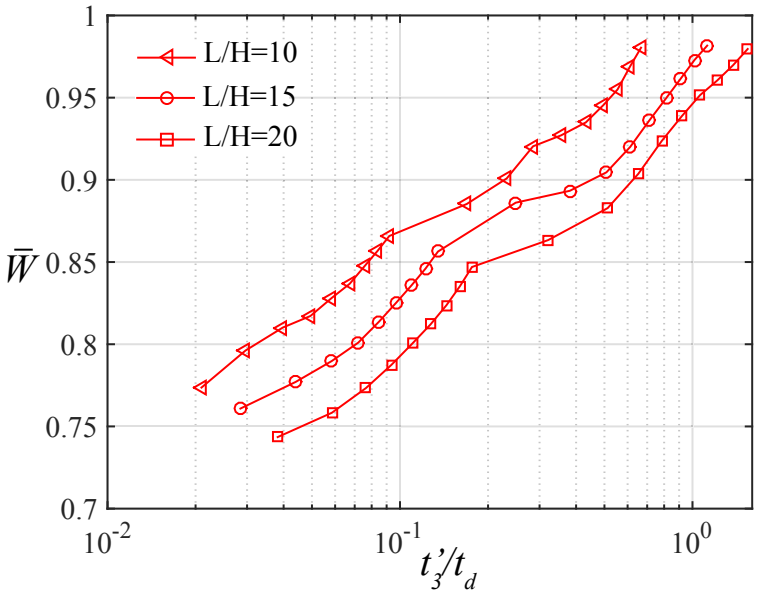

Figure 8: Variation of the displacement ratio $\bar{W}$ with FSI index β_s beams of different aspect ratio L/H deforming in mode I.

ρ_s is the density of gas behind the shock given by

$$\rho_s = \rho_a \frac{2\gamma_a + (\gamma_a + 1)\frac{p_s}{p_a}}{2\gamma_a + (\gamma_a - 1)\frac{p_s}{p_a}}, \tag{23}$$

and U_s is the shock speed given by

$$U_s = c_a \sqrt{\frac{(\gamma_a + 1)p_s}{2\gamma_a p_a} + 1}\ . \tag{24}$$

The shock wave is generated using the following parameters in Eqs. 8 and 9 so that all the beams deform only in mode I: $v_0/c_a = 5.6$, $d_0 = 0.05$ m and $d/d_0 = 79$.

Figure 6 shows a monotonic decrease of the displacement ratio $\bar{W}$ with velocity ratio $v_{\max}/U_s$ for all L/H. It shows that neglecting FSI would lead to an over-prediction of the maximum mid-span beam deflection – this is to be expected – and that this error increases with $v_{\max}/U_s$. Figure 7 plots $\bar{W}$ versus t_3'/t_d for different aspect ratio (L/H). Note that $t_3'/t_d \to \infty$ corresponds to the extreme case of impulsive loading where FSI effects may be neglected. As the time ratio t_3'/t_d decreases (or when the blast pulse becomes increasingly 'non-impulsive'), the error in the predicted structural response increases if FSI is ignored, as expected. To achieve a same 'amount' of FSI effect (say $\bar{W} = 0.8$, or 1-$\bar{W} = 0.2$), the beam with a higher L/H would take a longer time to reach its maximum mid-span deflection. This agrees with the analytical predictions by Jones [17] where it was shown that t_3' increases with L/H. Figure 8 shows that the error from ignoring FSI (or $1 - \bar{W}$) increases with β_s - this is

consistent with previous studies based on rigid, free-standing structures where it was shown that the beneficial effects of FSI can be harnessed through reducing the mass per unit area of a structure [2–4]. It is interesting to note that $\bar{W}$ is insensitive to L/H at very low β_s. This is because the mass per unit area of a beam is inversely proportional to β_s and, at very low β_s, the lack of beam motion leads to an insensitivity to L/H. As β_s increasing, the predictions for $\bar{W}$ become increasingly sensitive to L/H and the error of ignoring FSI increases with L/H (for a given β_s). This is unsurprising because, for the same mass per unit area, a longer beam develops a higher maximum mid-span velocity [7, 17], which alleviates the interface pressure leading to a greater FSI effect.

6. Effects of FSI on 'elasto-plastic' and 'rigid free-standing' beams

Here, we use the analytical model to investigate the uncoupled and fully-coupled dynamics of beams deforming in its three different modes. A parametric investigation is performed to evaluate the sensitivity of the maximum impulse transfer ($\bar{I}^T$) and external work done by the interface pressure ($\bar{E}^D$) to aspect ratio L/H and FSI index β_s. The maximum non-dimensional transmitted impulse $\bar{I}^T$ and external work done to a fully-clamped, elasto-plastic beam (Section 2.1) are defined, respectively, as follows:

$$\bar{I}^T = \max_{0\leq t'\leq t_d} [I^T(t')/I_i] \tag{25}$$

and

$$\bar{E}^D = \max_{0\leq t'\leq t_d} [E^D(t')/E_i]. \tag{26}$$

The aforesaid will be compared to its rigid free-standing counterpart of an identical mass per unit area. The maximum transmitted impulse and external work done - the superscript F denotes free-standing - are, respectively, given by [3]

$$\bar{I}^F = \lambda_R^{\beta_s(1+\beta_s)} \beta_s^{\beta_s/(1-\beta_s)} \tag{27}$$

and

$$\bar{E}^F = \lambda_R^{2\beta_s(1+\beta_s)} \frac{(1-e^{-\beta_s})^2}{2\beta_s}. \tag{28}$$

Note that λ_R (a non-dimensional parameter) is given by

$$\lambda_R = \gamma_R \left(\frac{C_R f_R}{\gamma_R} \right), \tag{29}$$

the non-dimensional parameter γ_R is

$$\gamma_R = 8 - 42 p_a \frac{\ln(1 + p_s/7p_a)}{p_s}, \tag{30}$$

and f_R is

$$f_R = \left(6\frac{p_s}{p_a} + 7 \right) \sqrt{\frac{(6 + C_R)\frac{p_s}{p_a} + 7}{\left(\frac{p_s}{p_a} + 7\right)\left((1 + 6C_R)\frac{p_s}{p_a} + 7\right)\left(C_R\frac{p_s}{p_a} + 7\right)}}. \tag{31}$$

6.1. Mode I (Figs. 9a & 9b)

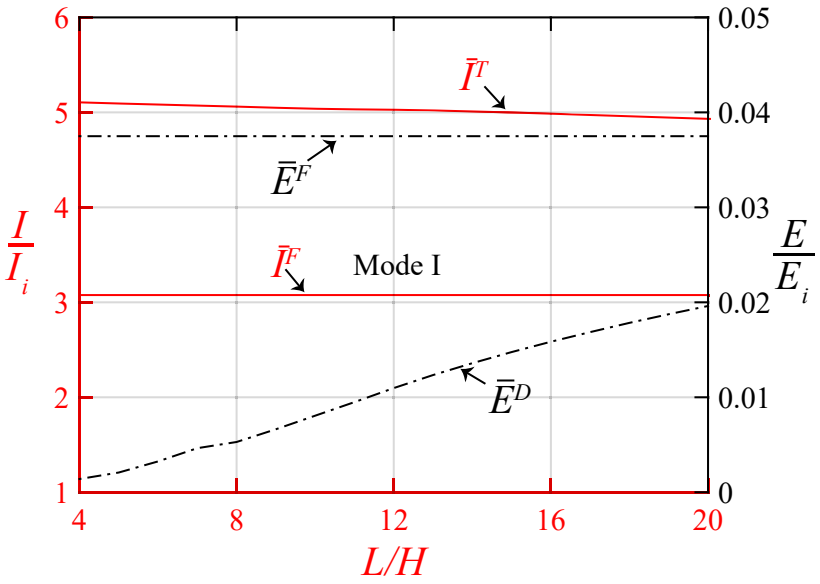

(a)

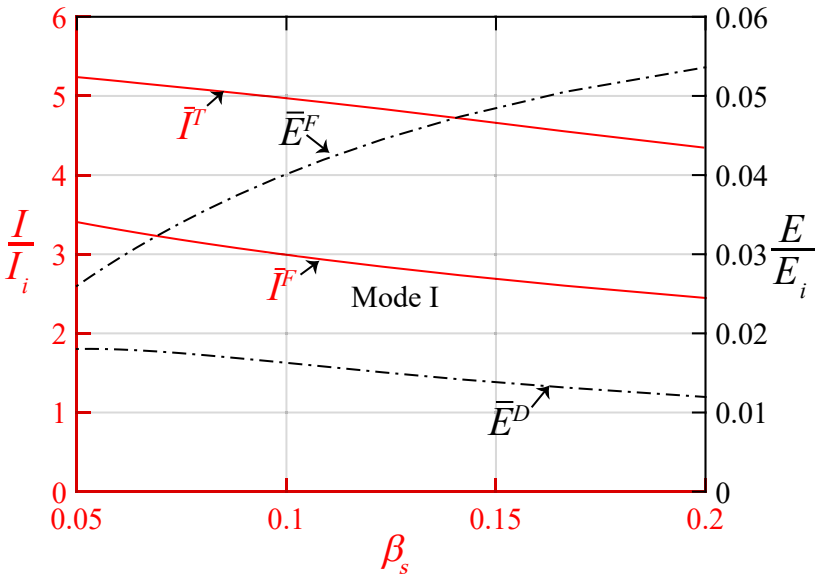

(b)

Figure 9: Variations of non-dimensional maximum impulse (—) and external work done (–.–) as a function of aspect ratio L/H and FSI index β_s, for beams deforming in mode I. In (a), all beams have a square cross-section of $H = B = 0.05$ m and a constant FSI index of $\beta_s = 0.084$; and, in (b), beams have identical aspect ratio of $L/H = 17$.

The following initial conditions were used in Eqs. 8 and 9 to ensure that all beams deform

only in mode I: $d_0 = 0.05$ m, $d/d_0 = 79$ and v_0/c_a=5.1. Figures 9a and 9b show how the non-dimensional impulses ($\bar{I}^T$ and $\bar{I}^F$) and external work done by the interface pressures ($\bar{E}^D$ and $\bar{E}^F$) vary as functions of aspect ratio L/H (for a constant $\beta_s = 0.084$) and FSI index β_s (for a constant $L/H = 17$), respectively. The results show that $\bar{I}^T$ reduces monotonically with L/H and β_s (a reduction of its mass per unit area). This is because increasing L/H or β_s leads to a higher maximum velocity that could be acquired by the elasto-plastic beam, resulting in greater alleviation of interface overpressure and, hence, greater effects of FSI. This also agrees with the findings in Fig. 8 where the error of ignoring FSI effect increases with L/H and/or β_s. For its free-standing counterpart, $\bar{I}^F$ is, as expected, only affected by the beam's mass per unit area ($\bar{I}^F$ reduces with β_s in Fig. 9b) and not its aspect ratio ($\bar{I}^F$ is invariant to L/H in Fig. 9a). In both Figs. 9a and 9b, a greater impulse is transmitted to the elasto-plastic beams, i.e. $\bar{I}^T > \bar{I}^F$, because the alleviation of interface overpressure is greater for free-standing beams due to their significantly higher velocity in the absence of resistance offered by the supports. The previous trend is reversed as the maximum external work done for the free-standing beams is significantly higher than its fully-clamped counterparts, i.e. $\bar{E}^F > \bar{E}^D$, since there are no supports to constrain the translational motion of the free-standing beams and, hence, it acquires a significantly higher displacement.

6.2. Modes II and III (Figs. 10a & 10b)

The initial conditions $d_0 = 0.05$ m, $d/d_0 = 79$ and v_0/c_a=5.1 were used in Eqs. 8 and 9 to ensure that beams deform in either mode II or III. Note that in mode III the ratio of the plastic work absorbed through shearing deformation to the total plastic work done reaches the critical ratio of $\beta_c = 0.45$ at failure [10]. It is evident that mode III deformation tends to occur for elasto-plastic beams with low L/H and high β_s. This is because decreasing L/H or increasing β_s leads to a somewhat smaller mid-span deflection which, in turn, results in a smaller proportion of plastic work absorbed through membrane deformation to the total plastic work done. Therefore the plastic work absorbed through shearing deformation to the total plastic work done β must be more significant, since it was shown in [7] that the plastic work absorbed through bending is negligible in mode III.

Figures 10a and 10b show that when complete detachment occurs, the maximum transmitted impulse $\bar{I}^T$ acquired by the beam decreases with L/H or β_s. Although these trends appear similar to those in mode I (Figs. 9a and 9b), the reduction of transmitted impulse is not a consequence of FSI effects since it was previously shown (see Figs 5b and 5c) that the peak transmitted impulse is unaffected by FSI if complete detachment occurs. Rather, this is due to early boundary failure by the elasto-plastic beams, i.e. increasing L/H or β_s leads to premature boundary failure, resulting in a greater reduction of the maximum non-dimensional impulse ($\bar{I}^T$) that is transmitted. The maximum non-dimensional impulse for a free-standing beam $\bar{I}^F$ always reduces with increasing β_s according to Eq. 27 as shown in Fig. 10b. Elasto-plastic beams deforming in mode II and III always have greater maximum transmitted impulse and lower maximum external work done by the interface pressure compared to their free-standing counterpart, i.e. $\bar{I}^T > \bar{I}^F$ and $\bar{E}^D < \bar{E}^F$, except

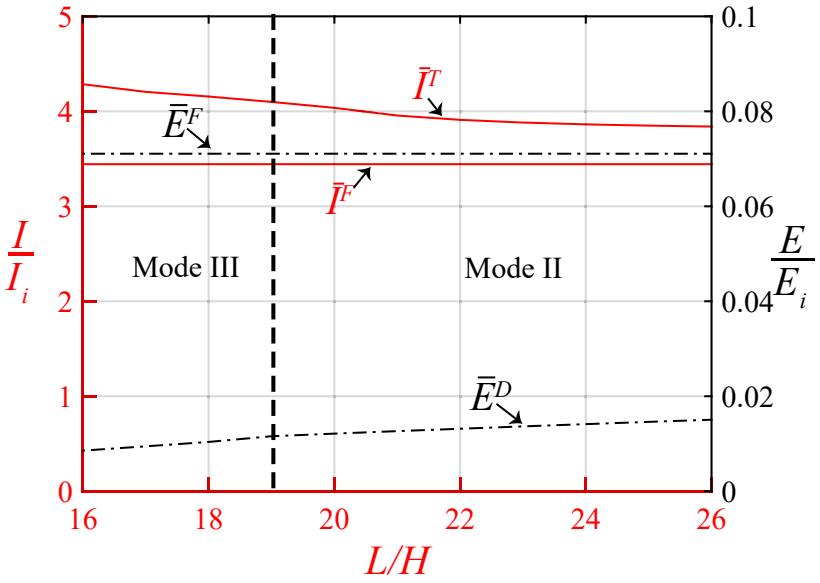

(a)

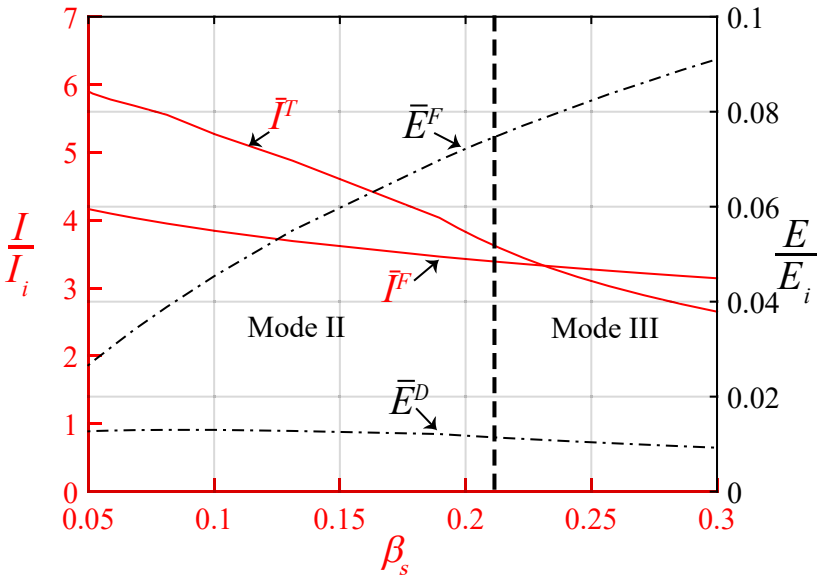

(b)

Figure 10: Variations of non-dimensional maximum impulse (—) and external work done (–.–) as a function of aspect ratio L/H and FSI index β_s, for beams deforming in modes II and III. In (a), all beams have a square cross-section of $H = B = 0.01$ m and a constant FSI index of $\beta_s = 0.189$; and, in (b), beams have identical aspect ratio of $L/H = 20$.

for a limited range of β_s in mode III where $\bar{I}^T < \bar{I}^F$. This is because, if β_s is high, complete detachment of the elasto-plastic beams occurs very early in its deformation history where simulation terminates, whilst its free-standing counterpart (if subjected to the same incident

shock wave) would continue to acquire impulse from the shock wave as it has yet to reach its maximum transmitted impulse.

7. Comparison of structural performance between underwater and air blasts

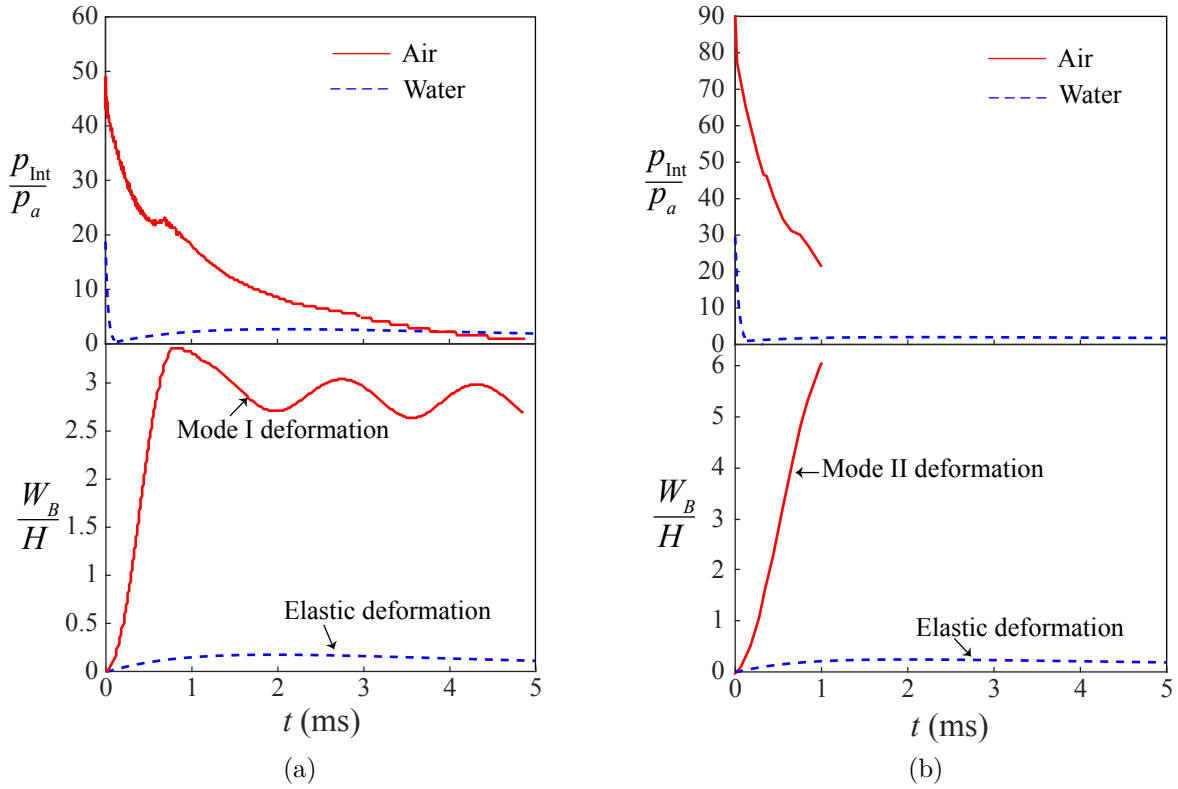

Figure 11: Predictions of temporal interface pressure and mid-span deflection of elasto-plastic beam subjected to an identical blast pulse in air and underwater. Results for air blast were from Figs. 5a and 5b

It is of interests to evaluate which medium (air or water) is more effective in mitigating the effects of blast loading for elasto-plastic structures subjected to a blast wave of identical intensity (i.e. same peak incident overpressure p_s and decay constant t_i). Predictions shown here for underwater blast are obtained using the analytical model developed by Yuan et al. [8] in a separate study. Figure 11 compares the interface pressure and mid-span deflection of an elasto-plastic beam subjected to an identical incident shock pulse in air and underwater. The incident overpressure in Figs. 11a and 11b can be characterised by $p_s = 1.00$ MPa and $t_i = 1.14$ ms, and $p_s = 1.55$ MPa and $t_i = 0.74$ ms, respectively. It can be seen in both figures that: (1) the peak interface overpressure in air is significantly higher than in water because of the non-linear compressibility effects of air; and (2) the interface pressure $p_{\text{Int}}(t)/p_a$ in water drops more dramatically than in air, as a result of greater alleviation of

interface pressure because of its significantly higher bulk modulus. Both contributes to the significantly less mid-span deflection predicted for an underwater blast compared to air, i.e. the elasto-plastic beam can develop mode I and even mode II deformation in air, but only deforms elastically in water. This demonstrates that an incompressible medium is able to better mitigate the effects of a blast wave for elasto-plastic structures subjected to the same incident wave.

A note of caution: the effects of standoff distance was omitted from the above analysis to highlight differences in the effects of FSI between the two media. Clearly, increasing standoff distance leads to attenuation of the peak incident overpressure and a longer pulse duration (see Figs. 3a and 3b for examples) in a compressible medium (air). By contrast, the shock wave travels without attenuation in an incompressible medium (water). Hence, the incident wave impinging on the structure will be different (unlike the above analysis) for the two media, i.e. the peak overpressure is significantly higher and pulse duration is smaller in underwater compared to an air blast. As a result, a structure may be more vulnerable to underwater explosion - than in an air blast - despite its superior capability of mitigating blast effects (as seen in Figs. 11a and 11b); the same was noted by Xue and Hutchinson [18] for sandwich structures.

8. Conclusion

The dynamic response of elasto-plastic beam subjected to intense air blast has been analysed. Numerical model developed by Yuan et al. [7] is used to predict the mid-span displacement, interface overpressure history, impulse transfer and external work done by the interface pressure for elasto-plastic beams deforming in three different modes of deformation. The key findings are listed below:

1. An uncoupled analysis (without consideration of FSI) suffices to determine the maximum value of the beam deflection, transmitted impulse and external work done by the interface pressure if a beam is deforming in either mode II or III. If FSI is ignored in mode I, the increasing over-prediction of the structural response is either a result of a higher beam's maximum speed relative to the shock speed or increasingly non-impulsive loading and a smaller mass per unit area.
2. In all three modes, increasing aspect ratio L/H or FSI index β_s always leads to a reduction in the maximum transmitted impulse through greater alleviation of the interface pressure.
3. Unlike a free-standing structure (beam), the external work done by the interface pressure is significantly lower if boundary conditions are included in the analysis. However, the presence of a physical boundary leads to greater momentum transfer except for exceptional cases in mode III where premature detachment from the support curtails the impulse transferred to the supported structure.
4. If a structure is subjected to an identical incident blast pulse, ignoring wave attenuation in air, then the underwater case is less likely to develop large inelastic deformation and complete detachment compared to its counterpart in air.

Acknowledgment

The authors are grateful to the Ministry of Defence, UK (Mr David Manley - DE&S Sea Systems Group), Lloyd's Register Marine (Dr Fai Cheng - Head of Strategic Research and Technology Policy) and QinetiQ (Mr Robert Ball - Structures & Survivability, Platform Design and Life Support IDT) for financial support.

References

[1] Taylor, G. I., The Pressure and Impulse of Submarine Explosion Waves on Plates. In *The Scientific Papers of Sir Geoffrey Ingram Taylor*, Vol. 3, Cambridge: Cambridge University Press, 1941.

[2] Kambouchev, N., Noels, L., Radovitzky, R., Nonlinear compressibility effects in fluid-structure interaction and their implications on the air-blast loading of structures, J. Appl. Phys. 100 (6) (2006) 063519.

[3] Kambouchev, N., Noels, L., Radovitzky, R., Numerical simulation of the fluid-structure interaction between air blast waves and free-standing plates, Comput. Struct. 85 (11) (2007) 923–931.

[4] Hutchinson, J. W., Energy and momentum transfer in air shocks, J. Appl. Mech. 76 (5) (2009) 051307–051307.

[5] Subramaniam, K. V., Nian, W., Andreopoulos, Y., Blast response simulation of an elastic structure: Evaluation of the fluid structure interaction effect, Int. J. Impact Eng. 36 (7) (2009) 965 – 974.

[6] Nian, W., Subramaniam, K. V. L., Andreopoulos, Y., Dynamic compaction of foam under blast loading considering fluid-structure interaction effects, Int. J. Impact Eng. 50 (2012) 29–39.

[7] Yuan, Y., Tan, P. J., Shojaei, K. A., Wrobel, P., Large deformation, damage evolution and failure of ductile structures to pulse-pressure loading, Int. J. Solids Struct. 96 (2016) 320 – 339.

[8] Yuan, Y., Tan, P. J., Shojaei, K. A., Wrobel, P., The influence of deformation limits on fluid structure interactions in underwater blasts, Int. J. Impact Eng. 101 (2017) 9 – 23.

[9] Menkes, S. B., Opat, H. J., Broken beams, Exp. Mech. 13 (11) (1973) 480–486.

[10] Shen, W. Q., Jones, N., A failure criterion for beams under impulsive loading, Int. J. Impact Eng. 12 (1) (1992) 101 – 121.

[11] Teich, M., Gebbeken, N., Analysis of FSI effects of blast loaded flexible structures, Eng. Struct. 55 (2013) 73 – 79.

[12] Neumann, J. V., Richtmyer, R., A method for the numerical computation of hydrodynamic shocks, J. Appl. Phys. 21 (1950) 232–237.

[13] Blom, F. J., A monolithical fluid-structure interaction algorithm applied to the piston problem, Comput. Methods Appl. Mech. Eng. 167 (3) (1998) 369 – 391.

[14] Blom, F. J., Leyland, P., Analysis of fluid-structure interaction on moving airfoils by means of an improved ale-method, in: Fluid Dynamics and Co-located Conferences, AIAA, 1997, pp. 97–1770. URL http://dx.doi.org/10.2514/6.1997-1770

[15] Drumheller, P. S., Introduction to Wave Propagation in Nonlinear Fluids and Solids, Cambridge: Cambridge University Press, 1998.

[16] Anderson, J., Fundamentals of aerodynamics, New York: McGraw-hill, 2001.

[17] Jones, N., Structural Impact, 2nd Edition, Cambridge University Press, 2012.

[18] Xue, Z., Hutchinson, J. W., Preliminary assessment of sandwich plates subject to blast loads, Int. J. Mech. Sci. 45 (4) (2003) 687 – 705.